Article

Proton Dynamics and Room-Temperature Ferroelectricity in Anilate Salts with a Proton Sponge

Sachio Horiuchi, Reiji Kumai, Yusuke Tokunaga, and Yoshinori Tokura

J. Am. Chem. Soc., **2008**, 130 (40), 13382-13391 • DOI: 10.1021/ja8032235 • Publication Date (Web): 10 September 2008

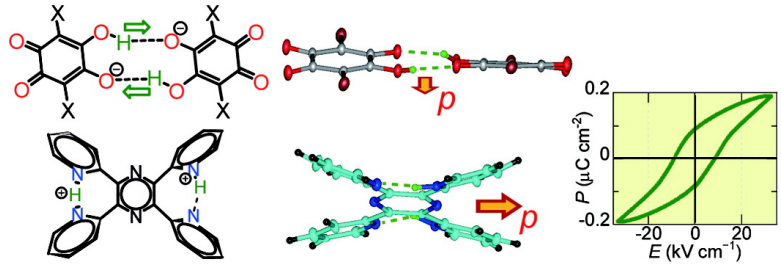

More About This Article

Additional resources and features associated with this article are available within the HTML version:

- Supporting Information
- Access to high resolution figures
- Links to articles and content related to this article
- Copyright permission to reproduce figures and/or text from this article

View the Full Text HTML

J|A|C|S
ARTICLES

Published on Web 09/10/2008

Proton Dynamics and Room-Temperature Ferroelectricity in Anilate Salts with a Proton Sponge

Sachio Horiuchi,*,† Reiji Kumai,*,† Yusuke Tokunaga,‡ and Yoshinori Tokura†,‡,§

Correlated Electron Research Center (CERC), National Institute of Advanced Industrial Science and Technology (AIST), Tsukuba 305-8562, Japan, Tokura Multiferroics Project, ERATO, JST, c/o AIST, Tsukuba 305-8562, Japan, and Department of Applied Physics, The University of Tokyo, Tokyo 113-8656, Japan

Received April 30, 2008; E-mail: s-horiuchi@aist.go.jp; r-kumai@aist.go.jp

Abstract: Ferroelectricity as well as characteristic proton-transfer dynamics are achieved by combining a 2,3,5,6-tetra(2′-pyridyl)pyrazine (TPPZ) molecule with anilic acids (H_2xa). Dielectric measurements revealed phase transitions at $T_c = 334$ and 172 K for bromanilate (Hba^-) and chloranilate (Hca^-) salts, respectively. The room-temperature ferroelectricity of the (H_2-TPPZ)$(Hba)_2$ crystal is evidenced by the slow polarization reversal with modest pyroelectricity. In accord with the observed large deuteration effect, synchrotron X-ray diffraction studies disclosed proton dynamics in an intramolecular N···H^+···N bond of the H_2-$TPPZ^{2+}$ dication and in an O−H···O^- hydrogen-bonded cyclic dimer of the *ortho*-quinoid Hxa^- anions. The disordered $(Hxa^-)_2$ dimer in two-fold orientation manifests its double-proton transfer process above T_c, whereas these protons are ordered in the ferroelectric phase. The H_2-$TPPZ^{2+}$ dication acts as a proton sponge by forming two intramolecular N···H^+···N hydrogen bridges between the pyridyl units with a very short N···N distance. The dication in the paraelectric state adopts a nonpolar geometry due to the delocalization of the protons over two sites in the respective N···H^+···N bonds. Below T_c, only one of the two protons gets localized, and the resultant acentric H_2-$TPPZ^{2+}$ ion generates the dipole moment responsible for the ferroelectricity.

1. Introduction

Anilic acids (or 2,5-dihydroxy-*p*-benzoquinones, H_2xa, see Chart 1) are strong dibasic acids that have long been utilized for the coordination of various transition metals, in supramolecular architecture, and as counteranions in conducting or paramagnetic charge-transfer complexes/salts[1] as well as for the spectrophotometric analysis of specific ions at the early stages.[2] Renewed interest in these compounds stems from recent discoveries of ferroelectricity resulting from hydrogen-bonding with organic dibasic bases such as phenazine (Phz)[3] and 5,5′-dimethyl-2,2′-bipyridine (55DMBP).[4] This is because organic ferroelectrics have been rare so far, in particular among the low-molecular-mass substances, in spite of their potential for prosperous use in information storage and as capacitors, piezoelectric/pyroelectric sensors, actuators, etc.[5,6] Furthermore, these new ferroelectrics[3,4] exhibit some attractive properties, such as large polarization and permittivity, at room temperature and operate at much lower voltage than that required for conventional ferroelectric polymers.[7]

Chart 1

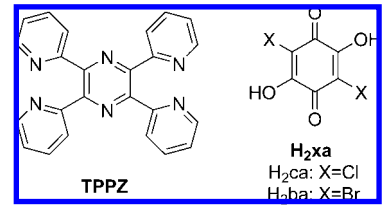

The ferroelectricity originates from the supramolecules comprising one-dimensional hydrogen-bonded chains, with the acid and base molecules alternating side-by-side. These intermolecular bonds are of heteronuclear origin, O−H···N (neutral) and/or N^+−H···O^- (ionic), in contrast to the homonuclear ones in the conventional ferroelectrics: O−H···O^- in the KH_2PO_4 (KDP) family[8] and N^+−H···N in ferroelectric diazabicyclo-[2.2.2]octane (dabco) salts.[9] The cooperative transfer[4] or displacement[10] of protons can cause polarization reversal of the supramolecular chains.

† National Institute of Advanced Industrial Science and Technology.
‡ ERATO, JST.
§ University of Tokyo.

(1) Kitagawa, S.; Kawata, S. *Coord. Chem. Rev.* **2002**, *224*, 11–34.
(2) Bertolacini, R. J.; Barney, J. E. *Anal. Chem.* **1957**, *29*, 281–283.
(3) (a) Horiuchi, S.; Ishii, F.; Kumai, R.; Okimoto, Y.; Tachibana, H.; Nagaosa, N.; Tokura, Y. *Nat. Mater.* **2005**, *4*, 163–166. (b) Horiuchi, S.; Kumai, R.; Tokura, Y. *J. Am. Chem. Soc.* **2005**, *127*, 5010–5011.
(4) (a) Kumai, R.; Horiuchi, S.; Okimoto, Y.; Tokura, Y. *J. Chem. Phys.* **2006**, *125*, 084715. (b) Horiuchi, S.; Kumai, R.; Tokura, Y. *Angew. Chem., Int. Ed.* **2007**, *46*, 3497–3501.
(5) Horiuchi, S.; Tokura, Y. *Nat. Mater.* **2008**, *7*, 357–366.
(6) Sworakowski, J. *Ferroelectrics* **1992**, *128*, 295–306.
(7) Furukawa, T. *Phase Trans.* **1989**, *18*, 143–211.
(8) Lines M. E.; Glass, A. M. *Principles and Applications of Ferroelectrics and Related Materials*; Oxford University Press: New York, 1977.
(9) Katrusiak, A.; Szafrański, M. *Phys. Rev. Lett.* **1999**, *82*, 576–579.
(10) Kumai, R.; Horiuchi, S.; Sagayama, H.; Arima, T.; Watanabe, M.; Noda, Y.; Tokura, Y. *J. Am. Chem. Soc.* **2007**, *129*, 12920–12921.

10.1021/ja8032235 CCC: $40.75

Table 1. Crystallographic Data Collection and Structural Refinement Information for $[H_2\text{-TPPZ}][Hxa]_2$

	$[H_2\text{-TPPZ}][Hba]_2$		$[H_2\text{-TPPZ}][Hca]_2$	
	FE, 200 K	PE, 370 K	FE, 100 K	PE, 295 K
formula	$C_{36}H_{20}Br_4N_6O_8$	$C_{36}H_{20}Br_4N_6O_8$	$C_{36}H_{20}Cl_4N_6O_8$	$C_{36}H_{20}Cl_4N_6O_8$
formula wt	984.21	984.21	806.40	806.40
crystal system	monoclinic	monoclinic	monoclinic	monoclinic
space group	*Cc* (No. 9)	*C*2/*c* (No. 15)	*Cc* (No. 9)	*C*2/*c* (No. 15)
a/Å	22.3407(7)	22.4282(13)	22.1980(11)	22.309(4)
b/Å	10.1916(3)	10.2454(6)	10.1502(4)	10.188(2)
c/Å	14.7991(9)	14.9797(15)	14.5046(8)	14.696(3)
β/deg	100.743(3)	99.797(7)	101.341(3)	100.228(6)
V/Å^3	3310.5(2)	3391.9(4)	3204.3(3)	3287.3(11)
ρ_{calc}/g cm^{-3}	1.975	1.927	1.671	1.629
Z	4	4	4	4
dimensions/mm	0.20 × 0.18 × 0.15	0.20 × 0.18 × 0.15	0.25 × 0.22 × 0.20	0.25 × 0.22 × 0.20
radiation	Synchrotron (λ = 0.99790 Å)	Synchrotron (λ = 0.99790 Å)	Synchrotron (λ = 0.68770 Å)	Synchrotron (λ = 0.68770 Å)
$2\theta_{max}$/deg	144.5	144.4	144.5	86.9
reflns used ($2\sigma(I) < I$)	9155	3312	11507	3272
no. of variables	568	397	568	397
R	0.024	0.027	0.022	0.032
R_w	0.031	0.040	0.024	0.040

In this study, we examined the 2,3,5,6-tetra(2′-pyridyl)pyrazine molecule[11] (TPPZ, Chart 1) as the counterpart of anilic acids to explore the extensive variety of H-bonding modes compatible with ferroelectricity. TPPZ allows various conformations[12,13] and accommodates six nitrogen atoms that were found to absorb as many as four protons on the pyridyl sites.[14] The divalent $H_2\text{-TPPZ}^{2+}$ ion can capture each proton between the two neighboring pyridine rings by forming a very short intramolecular $N^+-H\cdots N$ bond. This is why TPPZ is regarded as a proton sponge, analogous to 1,8-bis(dimethylamino)naphthalene (DMAN).[15] In a salt with chloranilic acid (H_2ca) or bromanilic acid (H_2ba), the TPPZ molecule absorbs two protons without participating in intermolecular H-bonds, while the mono-deprotonated anilic acids form a dimer. Here we report room-temperature ferroelectricity and novel phase transitions realized by proton dynamics on the two kinds of homonuclear H-bonds.

2. Experimental Section

2.1. Materials. Commercially available H_2ca, H_2ba, and TPPZ were purified by repeated gradient sublimation in a vacuum. Dark brown plates of $[H_2\text{-TPPZ}][Hxa]_2$ cocrystals were grown in methanol or ethanol by the diffusion of base and acid, which were separately settled in a sealed H-shaped glass tube. Deuteration of the H-bonds in $[H_2\text{-TPPZ}][Hxa]_2$ cocrystals was achieved by diffusion in 99.5%-deuterated CH_3OD (Aldrich) solution. Here, the degree of deuteration (80 and 85% for Hca and Hba salts, respectively) was obtained by recording the infrared vibrational spectra on a KBr disk; the amount of residual undeuterated species was estimated from the relative band intensity of undeuterated acid at 974 (Hca) or 955 cm^{-1} (Hba) by using the band of TPPZ at 555 cm^{-1} as an internal standard.

2.2. Dielectric Measurements. All the electric measurements described below were made on the as-grown single crystals with gold or silver paste painted on as the electrodes. The electric field was applied along the crystal [110] direction, with electrodes attached on the well-developed (110) crystal planes. The real and imaginary parts of the dielectric constant were measured with an LCR meter (HP 4284A). The temperature dependence of spontaneous polarization, namely the pyroelectricity, was examined by measuring the pyroelectric current with an electrometer (Keithley 6517). For the $[H_2\text{-TPPZ}][Hba]_2$ and $[H_2\text{-TPPZ}][Hca]_2$ crystals, the current under zero-field bias was measured during heating at a constant temperature sweep (1 K min^{-1}) once after the crystal was cooled from far above T_c (350 and 220 K, respectively) under direct current (dc) field bias of 2.7 and 7.9 kV cm^{-1}, respectively. Spontaneous polarization was obtained by integrating the current density with time. The electric polarization (*P*)−electric field (*E*) hysteresis curves were collected on a ferroelectrics evaluation system (Toyo Corp., FCE-1) consisting of a current/charge-voltage converter (Toyo Corp., Model 6252), an arbitrary waveform generator (Biomation 2414B), an analog-to-digital converter (WaveBook 516), and a voltage amplifier (NF Corp., HVA4321). The measurements were performed at room temperature with a high-voltage triangular wave field of 1 kV and various alternating frequencies.

2.3. Structure Analyses. Crystallographic data and experimental details are summarized in Table 1 for the $[H_2\text{-TPPZ}][Hba]_2$ and $[H_2\text{-TPPZ}][Hca]_2$ crystals. All the X-ray diffraction data at various temperatures were collected with a Rigaku DSC imaging plate system by using Si-double-crystal monochromatized synchrotron radiation (λ = 0.9979 or 0.6877 Å) at the beam line BL-1A of Photon Factory (PF), High-Energy Accelerator Research Organization (KEK). The monochromatized beam is focused using a bent cylindrical mirror made of Si crystal coated with Rh, with a focused beam size of 0.3 (vertical) × 0.7 (horizontal) mm. The crystal attached on a glass fiber was cooled or heated by flowing helium gas or nitrogen gas. The Rapid-AUTO program of Rigaku Corp. was employed for two-dimensional image processing. The Sir2004 program[16] was employed for the direct method. The CrystalStructure crystallographic software packages of Molecular Structure Corp. (MSC) and Rigaku Corp. were employed for the refinement of the structures. The final refinements of non-hydrogen atoms were done with anisotropic thermal factors. Crystallographic data for the structures reported in this paper are available as Supporting Information and have been deposited with the Cambridge Crystallographic Data Center.

In order to probe delicate changes in the H-bonding, we calculated the electron distribution by the maximum entropy

(11) Goodwin, H. A.; Lions, F. *J. Am. Chem. Soc.* **1959**, *81*, 6415–6422.
(12) (a) Bock, H.; Vaupel, T.; Näther, C.; Ruppert, K.; Havlas, Z. *Angew. Chem., Int. Ed. Engl.* **1992**, *31*, 299–301. (b) Greaves, B.; Stoeckli-Evans, H. *Acta Crystallogr. C* **1992**, *48*, 2269–2271.
(13) Padgett, C. W.; Pennington, W. T.; Hanks, T. W. *Cryst. Growth Des.* **2005**, *5*, 737–744.
(14) (a) Padgett, C. W.; Walsh, R. D.; Drake, G. W.; Hanks, T. W.; Pennington, W. T. *Cryst. Growth Des.* **2005**, *5*, 745–753. (b) Graf, M.; Stoeckli-Evans, H. *Acta Crystallogr. C* **1996**, *52*, 3073–3075.
(15) (a) Staab, H. A.; Saupe, T. *Angew. Chem., Int. Ed. Engl.* **1988**, *27*, 865–879. (b) Alder, R. W. *Chem. Rev.* **1989**, *89*, 1215–1223. (c) Llamas-Saiz, A. L.; Foces-Foces, C.; Elguero, J. *J. Mol. Struct.* **1994**, *328*, 297–324.
(16) Burla, M. C.; Caliandro, R.; Camalli, M.; Carrozzini, B.; Cascarano, G. L.; De Caro, L.; Giacovazzo, C.; Polidori, G.; Spagna, R. *J. Appl. Crystallogr.* **2005**, *38*, 381–388.

method (MEM).[17] The MEM calculation was performed using the ENIGMA program[18] at a resolution of 256 × 128 × 128 pixels. In order to extract the electron density distribution of the hydrogen atoms on the OH···O and NH···N bonds, we also performed calculations called the differential MEM analysis.[19] As the reference, the MEM analysis was applied to the structural factors which were calculated from the atomic parameters with target hydrogen atoms omitted. The differential electron distribution is obtained by subtracting these reference data from the total density distribution.

With use of the same synchrotron X-ray source, the absolute structure and degrees of polarity reversal in the ferroelectric phase were examined on the basis of the Flack's parameters[20] in the analysis of the single crystals under an electric field applied along the crystal [110] direction. Under a dc bias field of 1.3 kV cm^{-1}, the $[H_2$-TPPZ$][Hba]_2$ and $[H_2$-TPPZ$][Hca]_2$ crystals were poled while cooling from 380 and 295 K (above the phase transition temperature, T_c) to 200 and 100 K ($<T_c$), respectively. The gold wires (10 μm diameter) were carefully attached to the crystal with silver paint to minimize their obstructive absorption and diffraction of the X-ray as well as their thermal conduction.

3. Results and Discussion

3.1. General Scope of $[H_2$-TPPZ$^{2+}][Hxa^-]_2$. According to the crystal structure analysis, the two compounds are formulated as $[H_2$-TPPZ$^{2+}][Hxa^-]_2$. Their proton-transferred character is also confirmed by optical spectroscopy measurements. Further details are provided as Supporting Information. The overall infrared absorption spectra (Figure S1) are clearly distinct from the superposition of the vibrational spectra of neutral components H_2xa and TPPZ. Therefore, they cannot be regarded as neutral cocrystals. Rather, the vibrational spectra around 1500−1700 cm^{-1} are very similar to those of a proton-transferred monovalent Hxa^- form. They exhibit an intense band around 1540−1550 cm^{-1}, which is associated with the stretching vibration of the deprotonated C−O bond. Further evidence for the monovalent Hxa^- anion was obtained from the visible spectra (Figure S2), in which the Hxa^- or other (H_2xa and xa^{2-}) species can be distinguished by the presence or absence of an intense absorption at 2.4 eV.[4a] The two TPPZ salts exhibited the corresponding absorption band around 2.2−2.4 eV in both the solid state and the acetonitrile solution.

According to the X-ray diffraction measurements, the two TPPZ salts show the isomorphous unit cell of a *C*-centered monoclinic crystal system (Table 1), containing diprotonated H_2-TPPZ^{2+} dications and deprotonated Hxa^- monoanions in 1:2 ratio. Figure 1 represents the crystal structure of $[H_2$-TPPZ$][Hba]_2$ determined at $T = 200$ K. The unit cell is large, accommodating as many as four H_2-TPPZ^{2+} dications and eight Hxa^- monoanions ($Z = 4$). The monoanions form a hydrogen-bonded $[Hxa^-]_2$ dimer, as shown by the dotted lines in the figure. The H_2-TPPZ^{2+} dication and $[Hxa^-]_2$ dimer form an alternating π-molecular stack along the crystallographic *c*-direction. All the pronounced dielectric anomalies and ferroelectricity discussed below were observed with the electric field applied parallel to the crystallographic [110] direction.

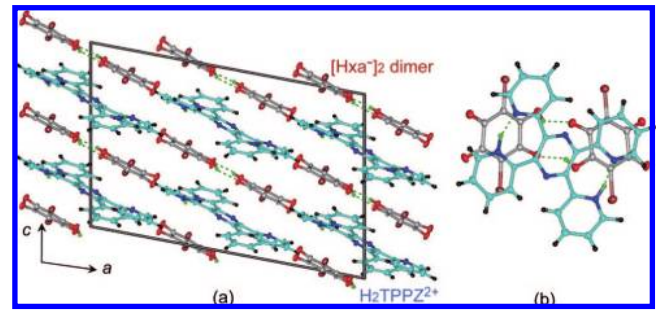

Figure 1. Crystal structure of the $[H_2$-TPPZ$][Hba]_2$ crystal at $T = 200$ K. (a) Molecular packing viewed along the crystallographic *b*-axis. (b) Molecular overlap of the $\pi-\pi$ stacking H_2-TPPZ^{2+} dication and $[Hba^-]_2$ dimer. Green dotted lines represent the intermolecular hydrogen bonds in the $[Hba^-]_2$ dimer and the intramolecular hydrogen bonds of H_2-TPPZ^{2+}.

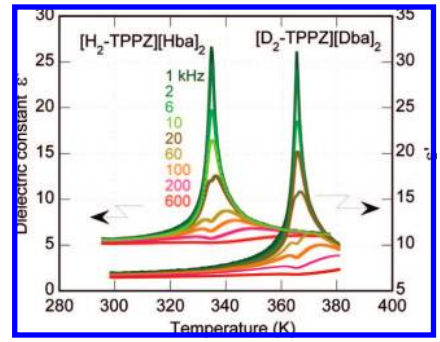

Figure 2. Temperature-dependent dielectric constant ϵ' of $[H_2$-TPPZ$][Hba]_2$ and its deuterated crystals at various frequencies.

3.2. Dielectric Properties and Room-Temperature Ferroelectricity of $[H_2$-TPPZ$^{2+}][Hba^-]_2$. The complex dielectric constant $\epsilon(\omega) = \epsilon' + i\epsilon''$ was measured for both TPPZ salts with various frequencies $f = \omega/2\pi$ from 600 Hz to 1 MHz. For the Hba salt, the real part of dielectric constant ϵ' showed the peak anomalies with pronounced frequency dependences (Figure 2). The phase transition is well-defined at 334 K, with a sharp peak maximum in the low-frequency data. A characteristic behavior of ferroelectrics appears in the low-frequency dielectric constant obeying the Curie−Weiss law,

$$\varepsilon' = \frac{C}{T-\theta} + \varepsilon_a \qquad (1)$$

The temperature-independent ϵ_a is 5.3 from the fitting to the data. Compared with the previous ferroelectric cocrystals of anilic acids, the magnitude of the peak maximum (30) and Curie constant C (39.5 K) are about 1 or 2 orders of magnitude smaller, indicating the weak polarization. The phase transition is of weak first order or continuous because temperature hysteresis is not discernible and also because the Weiss temperature $\theta = 333.3$ K almost coincide with the Curie point T_c within 0.5 K.

Considering the crystal symmetry as discussed below, the spontaneous polarization vector should be parallel to the *ac* plane. All the above dielectric anomalies were actually obtained with the alternating current (ac) electric field applied parallel to the crystallographic [110] direction, whereas they are almost silent in the measurements along the *c*-direction. This implies that the polarization is nearly parallel to the *a*-direction. For the direct proof of ferroelectricity, we measured the $P-E$ hysteresis loop along the [110] direction of the $[H_2$-TPPZ$][Hba]_2$

(17) Sakata, M.; Sato, M. *Acta Crystallogr. A* **1990**, *46*, 263–270.
(18) Tanaka, H.; Takata, M.; Nishibori, E.; Kato, K.; Iishi, T.; Sakata, M. *J. Appl. Crystallogr.* **2002**, *35*, 282–286.
(19) (a) Kiyanagi, R.; Kojima, A.; Hayashide, R.; Kimura, H.; Watanabe, M.; Noda, Y.; Mochida, T.; Sugawara, T.; Kumazawa, S. *J. Phys. Soc. Jpn.* **2003**, *72*, 2816–2821. (b) Nishibori, E.; Nakamura, T.; Arimoto, M.; Aoyagi, S.; Ago, H.; Miyano, M.; Ebisuzaki, T.; Sakata, M. *Acta Crystallogr. D* **2008**, *64*, 237–247.
(20) Flack, H. D. *Acta Crystallogr. A* **1983**, *39*, 876–881.

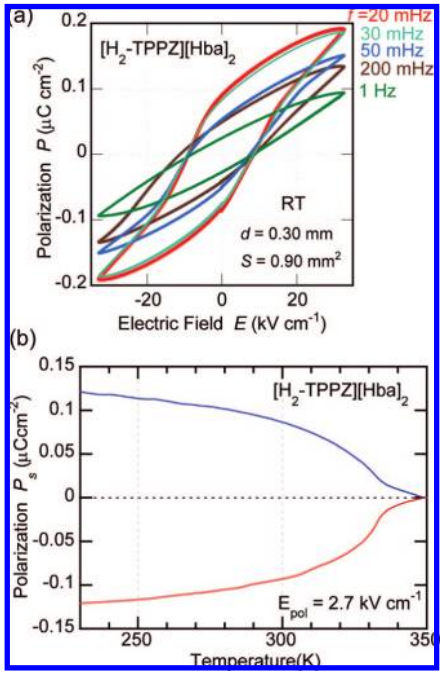

Figure 3. Room-temperature ferroelectricity of the $[H_2\text{-TPPZ}][Hba]_2$ crystal. (a) Hysteresis loops of electric polarization measured with ac electric field of various frequencies. (b) Temperature dependence of spontaneous polarization obtained by the pyroelectric current measurements.

crystal at room temperature (Figure 3a) using the ac field of a triangular waveform. Satisfactory measurements required application of a higher field (>30 kV cm^{-1}) and much lower ac frequency (20−30 mHz) than those on other ferroelectric cocrystals of anilic acid. The $P-E$ curves collapse with increasing frequency beyond 50 mHz. That is, the polarization reversal is too slow to follow even such a low-frequency field so as to complete the ideal loop. This fact should be closely related with very slow dielectric relaxation in the paraelectric phase, as shown below. The hysteresis loop at 20 mHz gave a coercive field of 8.8 kV cm^{-1}, which is higher than those of other ferroelectric cocrystals of anilic acid[5] but still much lower than those of ferroelectric polymers.[7] The remanant polarization is small (0.086 μC cm^{-2}).

To obtain additional evidence of ferroelectricity, we performed pyroelectric charge measurements, in which the crystal can be poled over a sufficiently long time period during cooling from above the Curie temperature. This quasi-thermodynamic method is also advantageous in poling samples with temperature passing through T_c, where the coercive field should be minimized. Figure 3b displays the temperature dependence of spontaneous polarization, which was obtained by integrating the pyroelectric current density. The polarity reversal was confirmed by the inversion of current flow upon the reversal of applied field. The spontaneous polarization was found to increase steeply just below T_c upon cooling. These results prove the room-temperature ferroelectricity. Compared with previous ferroelectric cocrystals of anilic acids,[5] the maximum spontaneous polarization, $P_s = 0.12$ μC cm^{-2}, is lower by about 1 order of magnitude. The room temperature value of 0.09 μC cm^{-2} agrees well with the remanent polarization of $P-E$ hysteresis measured at the lowest ac frequency ($f = 20-30$ mHz). In relation to the observed small Curie constant, the P_s is transformed to the dipole moment per formula unit, $\mu_s = P_s/N = 0.99 \times 10^{-30}$ C·m, using the density of dipoles, $N = 1.208 \times 10^{27}$ m^{-3}, and is found to be comparable to the effective paraelectric moment, $\mu_C = 2.0 \times 10^{-30}$ C·m, given by $C = N\mu_C^2/k_B\epsilon_0$ (k_B, Boltzmann constant; ϵ_0, permittivity of vacuum). The ratio $\mu_C/\mu_s = 2$ is the typical value for ferroelectrics (1−2),[21] indicating the proper ferroelectric transition in which the spontaneous polarization represents the order parameter.

Finally, we discuss the frequency dependence of dielectric properties (Figure 2), in which the real part ϵ' is diminished and its peak maximum at T_c finally turns to a flattened line with increasing frequency. At each temperature near T_c, the imaginary part ϵ'' as a function of ac frequency (Figure 4a) exhibits a broad peak just where the ϵ' drops most steeply. This observation is characteristic of the Debye-type dielectric relaxation, in which the reorientation of dipoles cannot respond to the applied ac electric field with high frequency exceeding a relaxation rate $1/\tau$. This mechanism is expressed as[8]

$$\varepsilon'(\omega) = \frac{\varepsilon_0 - \varepsilon_\infty}{1 + \omega^2\tau^2} + \varepsilon_\infty \tag{2}$$

$$\varepsilon''(\omega) = \frac{(\varepsilon_0 - \varepsilon_\infty)\omega\tau}{1 + \omega^2\tau^2} \tag{3}$$

Here, τ is the relaxation time and the frequency at $\omega\tau = 1$ gives maximal ϵ. The terms ϵ_0 and ϵ_∞ are the static and high-frequency dielectric constants, respectively. From eqs 2 and 3, we can derive the relation,

$$\left\{\varepsilon' - \frac{\varepsilon_0 + \varepsilon_\infty}{2}\right\}^2 + \varepsilon''^2 = \left\{\frac{\varepsilon_0 - \varepsilon_\infty}{2}\right\}^2 \tag{4}$$

The Cole−Cole diagram (Figure 4b) exhibits semicircles for temperatures above T_c, representing this mechanism with a single relaxation. On the other hand, more relaxation mechanisms are suggested by a complicated curve below T_c. The relaxation frequency $1/2\pi\tau$ was obtained from the fitting data to eq 3 for temperatures above T_c. It is proportional to $(T - T_c)$ near T_c and bends upward far above T_c (Figure 4c). Very similar dielectric properties are observed as the critical slowing-down in the typical order−disorder (OD)-type ferroelectrics such as $NaNO_2$.[22] For the $[H_2\text{-TPPZ}][Hba]_2$, the overall relaxation rate is about 3 orders of magnitude slower than that of $NaNO_2$.

3.3. Dielectric Properties and Ferroelectricity of $[H_2\text{-TPPZ}^{2+}][Hca^-]_2$. The dielectric response of $[H_2\text{-TPPZ}][Hca]_2$ and its deuterated salts is minute, with some contrasting behaviors as compared to the Hba salt (Figure 5). A tiny drop of the dielectric constant ϵ' appears reversibly at 169 and 175 K upon cooling and heating, respectively, in the Hca salt (Figure 5a). This temperature hysteresis with a width of 6 K indicates the first-order phase transition. The deuterated $[D_2\text{-TPPZ}][Dca]_2$ salt also exhibits a similar kink-like anomaly (Figure 5c) but without perceptible temperature hysteresis at $T_c = 240$ K, which is elevated by as much as 68 K upon deuteration. The absence of Curie−Weiss behavior as well as no anomalies in ϵ'' differs from the typical characteristics of a ferroelectric.

According to the pyroelectric measurements, a discontinuous jump appears in spontaneous polarization at the temperature (175 K) coincident with the dielectric anomaly on a heating run (Figure 6). This fact is evidence again the first-order nature of the phase transition, in contrast to the almost continuous character of the Hba salt. The ferroelectric nature was confirmed by the inversion of current flow upon the

(21) Tokunaga, M. *J. Phys. Soc. Jpn.* **1988**, *57*, 4275–4283.
(22) Hatta, I. *J. Phys. Soc. Jpn.* **1968**, *24*, 1043–1053.

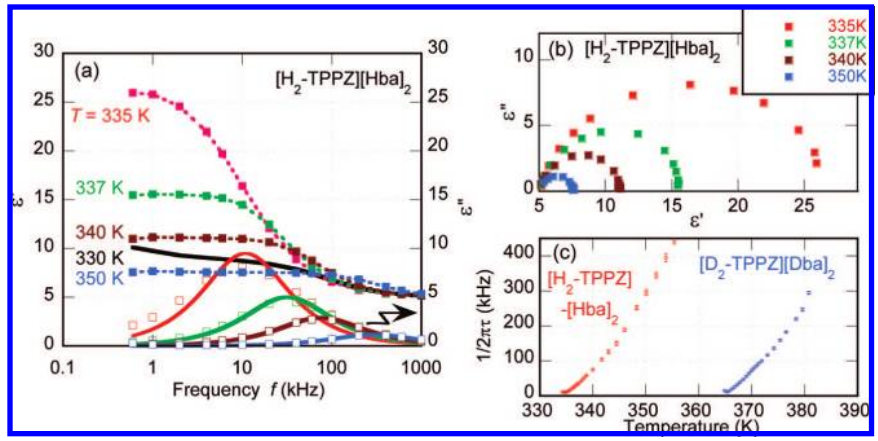

Figure 4. Dielectric relaxation properties of the $[H_2\text{-TPPZ}][Hba]_2$ crystal. (a) Frequency dependence of the real ϵ' (solid squares) and imaginary parts ϵ'' (open squares) of complex dielectric constant at various temperatures. Dotted and solid curves represent the fit to the Debye-type relaxation model. (b) Relation between ϵ' and ϵ'' (the Cole−Cole diagram). (c) Temperature dependence of the relaxation frequency $1/2\pi\tau$ for $[H_2\text{-TPPZ}][Hba]_2$ and its deuterated crystals. Vertical errors bars result from the fitting to the Debye-type relaxation model.

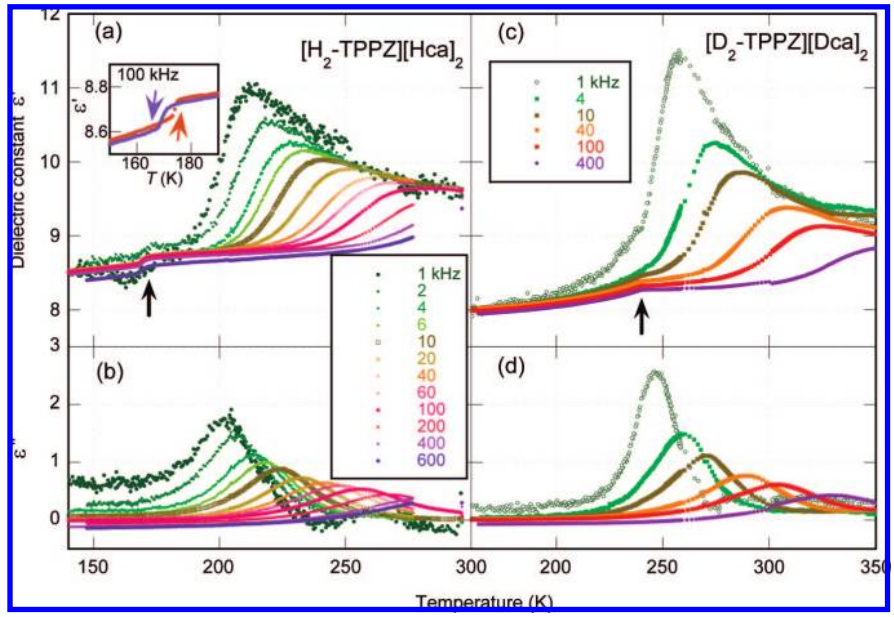

Figure 5. Temperature dependence of the complex dielectric constant [real part ϵ' (panels a,c) and imaginary part ϵ'' (b,d)] of $[H_2\text{-TPPZ}][Hca]_2$ (a,b) and its deuterated crystal (c,d) at various frequencies. The color and black arrows indicate the thermal process and the phase transition temperature, respectively.

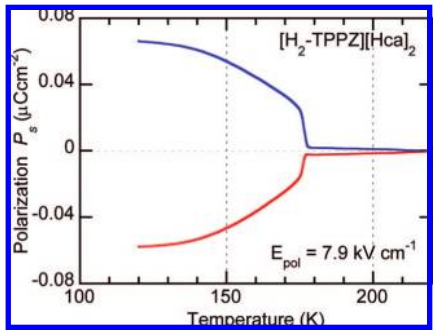

Figure 6. Temperature dependence of spontaneous polarization obtained by pyroelectric current measurements on the $[H_2\text{-TPPZ}][Hca]_2$ crystal.

reversal of applied field. The spontaneous polarization is further diminished to 0.062 μC cm^{-2} compared with the Hba salt.

$[H_2\text{-TPPZ}][Hca]_2$ and its deuterated form also exhibit a frequency dispersion with rounded peaks in ϵ' and ϵ'' (Figure 5). These broad maxima, appearing far above the transition points, shift toward higher temperature with increasing frequency and are only artifacts due to the dielectric relaxation phenomena, not signs of phase transition. At first glance, this behavior is reminiscent of a relaxor,[23] in which polar microdomains prevent the evolution of long-range order for macroscopic polarization in the absence of electric field. Although the pyroelectric discharge should be expected also for the case of a field-cooled relaxor, it was not perceivable at all above T_c (Figure 6), including the $T < 200$ K region where the dielectric relaxation is apparent in the Hca salt. Therefore, this compound cannot be a relaxor.

These dielectric relaxations approximately obey the above Debye-type formula (eqs 2 and 3), and so the relaxation time at each temperature was similarly obtained by fitting the data

(23) Cross, L. E. *Ferroelectrics* **1987**, *76*, 241–267.

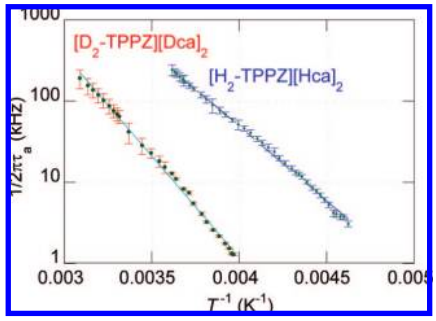

Figure 7. Arrhenius plot of the relaxation frequency $1/2\pi\tau$ as a function of inverse temperature for $[H_2\text{-TPPZ}][Hca]_2$ and its deuterated crystals. Vertical bars represent the errors resulting from the fitting to the Debye-type relaxation model. Linear blue lines are least-squares fits to eq 5 for the thermal activation behavior.

to eq 3. As shown in Figure 7 by the relaxation frequency $1/2\pi\tau$ as a function of inverse temperature, the linear relation in the Arrhenius plot,

$$1/2\pi\tau = A\exp\left(-\frac{E_a}{k_B T}\right) \quad (5)$$

manifests the relaxation of a thermally activated type. The activation energies E_a for dielectric relaxation are as high as 0.366 (4238 K) and 0.497 eV (5760 K) for the Hca and Dca salts, respectively. The relaxation rate can be determined only for temperatures far above T_c because it decreases rapidly below the lowest measured frequency on approaching T_c. The distinct appearance of dielectric properties of the Dca compared to those of the Hba salts can be merely ascribed to the different time scales of dipole-inversion dynamics relative to the dielectric measurement. In this case, experiments with ac frequency lower by a few orders of magnitude would revive both the critical slowing in the vicinity of T_c and the Curie−Weiss behavior on approaching the order−disorder transition. These facts imply extremely slow dynamics of polarization.

3.4. General Structural Features of $[H_2\text{-TPPZ}][Hxa]_2$. All the diffraction data were collected using a synchrotron X-ray source to determine the electron density distribution on the hydrogen bonds by the MEM analysis. At room temperature, the $[H_2\text{-TPPZ}][Hca]_2$ salt crystallizes in a centrosymmetric structure with a space group $C2/c$, whereas its Br analogue belongs to the acentric subgroup (space group Cc). Considering their phase transition temperatures, these two crystal structures represent the respective high- and low-temperature phases, respectively. The observed acentric structure of $[H_2\text{-TPPZ}][Hca]_2$ at $T = 100$ K $< T_c$ and centric one of $[H_2\text{-TPPZ}][Hba]_2$ at $T = 370$ K $> T_c$ proved the isomorphous structural transformations of the two compounds. Therefore, the symmetry-breaking without multiplication of the unit cell characterizes the ferroelectric nature of this phase transition. Hereafter, these structures will be called paraelectric phase (PE) and ferroelectric phase (FE) structures, respectively.

In the FE crystal structure, as exemplified in Figure 1 by that of $[H_2\text{-TPPZ}][Hba]_2$ at $T = 200$ K, the asymmetric unit comprises one $[Hba^-]_2$ dimer (Figure 8a) and one $H_2\text{-TPPZ}^{2+}$ dication (Figure 8b). In the PE structure, on the other hand, the asymmetric unit contains one Hxa^- anion and half of the $H_2\text{-TPPZ}^{2+}$ dication at the inversion symmetry. A two-fold rotation axis emerges across the $[Hxa^-]_2$ dimer on the transformation to the PE structure. According to the structural analysis, the phase transition significantly changes the hydrogen-bonding and

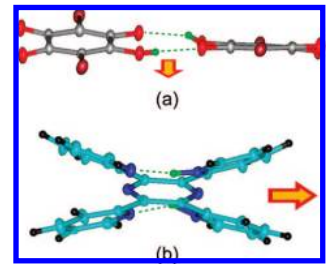

Figure 8. (a) $[Hxa^-]_2$ dimer and (b) $H_2\text{-TPPZ}^{2+}$ dication, showing the hydrogen bonds (green dotted lines) and the direction of dipole moments (brown arrows).

Table 2. Hydrogen Bonding and Molecular Geometry of $[H_2\text{-TPPZ}][Hxa]_2$

	$[H_2\text{-TPPZ}][Hba]_2$		$[H_2\text{-TPPZ}][Hca]_2$	
	FE 200 K	PE 370 K	FE 100 K	PE 295 K
		$[Hxa^-]_2$ Dimer		
O···O⁻/Å	2.627(2)	2.625(3)	2.602(1)	2.607(3)
	2.684(2)	2.687(4)	2.651(1)	2.663(3)
O−H/Å	0.78(4)	0.79(4)	0.88(2)	0.77(4)
	0.90(4)	0.86(3)	0.71(2)	0.87(5)
twist angle/°	17.40(9)	15.83(15)	18.08(3)	15.74(14)
		$H_2\text{-TPPZ}^{2+}$ Dication		
$N_{1a}\cdots N_{2a}$/Å	2.529(1)	2.545(1)	2.5347(7)	2.551(1)
N_{1a}−H/Å	1.03(2)	1.15(2)	1.25(2)	1.20(2)
$N_{1b}\cdots N_{2b}$/Å	2.557(1)	−	2.5694(7)	−
N_{2b}−H/Å	0.93(3)	−	1.04(2)	−
$\angle CN_{1a}C$/°	121.88(9)	120.9(1)	122.04(5)	122.12(8)
$\angle CN_{2a}C$/°	121.74(9)	121.73(9)	122.00(6)	121.14(9)
$\angle CN_{1b}C$/°	120.3(1)	−	120.20(5)	−
$\angle CN_{2b}C$/°	122.5(1)	−	122.97(6)	−
ψ_{1a}/° [a]	18.1(2)	21.92(16)	16.65(7)	19.87(9)
ψ_{2a}/°	17.9(2)	20.63(17)	17.15(7)	19.95(9)
ψ_{1b}/°	23.4(2)	−	21.89(7)	−
ψ_{2b}/°	24.1(2)	−	23.91(7)	−

[a] The twisting angle ψ between the pyrazine and pyridine rings is derived from the NCCN torsion angle. See Chart 2 for notation of pyridyl rings 1 and 2 on the $H_2\text{-TPPZ}^{2+}$ dication.

Scheme 1. Double-Proton-Transfer Process in the $[Hxa^-]_2$ Dimer

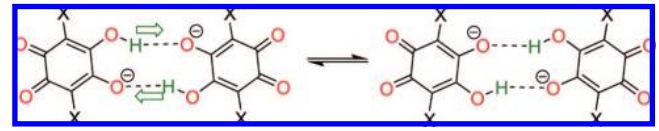

molecular geometries for both the $[Hxa^-]_2$ dimer and the $H_2\text{-TPPZ}^{2+}$ dication, which will be discussed separately in the following.

3.5. Structural Changes of $[Hxa^-]_2$ Dimer. 3.5.1. Ordered Configuration in Ferroelectric (FE) Structure. Table 2 summarizes the geometric parameters of the hydrogen-bonded $[Hxa^-]_2$ dimers for the two compounds. There are two hydrogen bonds with very short O···O distance (2.60−2.68 Å), as shown by dotted line in Scheme 1. Since the coplanar dimer addresses a center of inversion, as seen in the same scheme, one cannot expect a large polarization solely from small dihedral angle (17−18°) between two Hxa^- anions in the actual crystals.

According to the lengths of four C−O bonds, the Hxa^- anion adopts a novel *ortho*-quinoid form rather than the *para*-quinoid tautomer typical of the monovalent form.[24,25] This observation indicates that these two tautomeric π-conjugated forms can be flexibly interchanged,[26] depending on the nature of the intermolecular interactions. The hydrogen-bonded dimeric unit

Chart 2. Hydrogen-Bonding Geometry and Twisting of the Pyridyl Rings with Numbering Scheme in the H_2-$TPPZ^{2+}$ Molecule

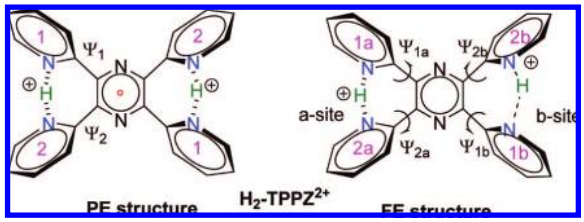

constructs a ring, which comprises a total of 10 atoms including two protons diagonally located (Scheme 1). This hydrogen-bonded ring reminds us of the well-known carboxylic acid dimer with an 8-atom ring. In the $[Hxa^-]_2$ dimer, the C═O bonds with lengths of 1.22−1.23 Å appear on the outside oxygen atoms, whereas the O−H group can face the negatively charged $C-O^-$ group (bond distance of 1.25−1.26 Å), forming two ionic $O-H\cdots O^-$ hydrogen bonds. As far as we know, based on a similar dimer in previously reported cocrystals, the monovalent Hxa^- are always crystallized as the *para*-quinoid tautomer. With this tautomer, the negatively charged $C-O^-$ group orients outside the dimer, whereas the dimer comprises the neutral $O-H\cdots O{=}C$ bonding. This is because the $C-O^-$ groups form ionic $N^+-H\cdots O^-$ bonds with bases in the neighborhood. In the present case, by contrast, there is no intermolecular H-bond with H_2-$TPPZ^{2+}$ dication. The reason for the preference of the *ortho*-quinoid form then would be the strengthened H-bonding owing to its ionic nature relative to the neutral bonds between the *para*-quinoid molecules.

3.5.2. Disordered Configurations in Paraelectric (PE) Structure. In the PE structure of the two compounds, a two-fold rotation axis emerges between two Hxa^- molecules, and this C_2 symmetry demands each proton be evenly disordered on the two oxygen atoms. The unusually large thermal ellipsoids of the Hxa^- molecule are indicative of the static or dynamical disorder. Electron density distributions including these disordered atoms were examined in detail by the MEM analysis. The electron density contour map shown in Figure 9a clearly exhibits doubly split maxima in the disordered state, especially near the hydrogen bonds. The disordered atoms including the hydrogen could be refined at two separate positions with equal probability (0.5), as shown in Figure 9b. The picture of the disordered hydrogen locations over doubly split sites was further scrutinized by the differential MEM analysis,[19] which extracted the electron density distribution for these hydrogen atoms according to the MEM calculation procedures described in the Experimental Section. The contour maps shown in Figure 10 were calculated on a least-squares plane defined by the adjacent oxygen atoms. Whereas the two ordered hydrogen atoms appear in the FE structure (Figure 10a), the PE structure discloses a quartet of peak maxima with nearly equal height (Figure 10b), consistent with the results of least-squares refinement. Their π- and hydrogen-bond geometries are well explained by the two-fold orientational disorder, as specified by the greenish and bluish configurations in Figure 10b. These two configurations of the dimer are related to one another by double-proton transfer,

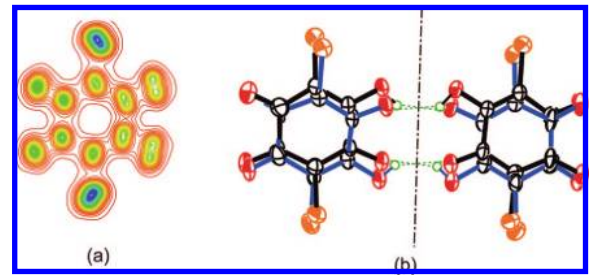

Figure 9. Thermally disordered $[Hca^-]_2$ dimer in the PE structure (T = 295 K). (a) Contour images of the electron density on the molecular plane deduced from the maximum entropy method. (b) Thermal ellipsoid plot of the dimer with two-fold configurations. The broken line represents a two-fold rotation axis.

which is accompanied by simultaneous molecular rotation so as to maintain the quasi-linear $O-H\cdots O$ bond as seen in Scheme 1. Accordingly, the ferroelectric transition transforms the H-bonded dimer from the dynamically disordered to the ordered state.

3.6. Structural Changes of H_2-$TPPZ^{2+}$ Dication. For the TPPZ molecule, there are at least five different protonated species, varying from neutral to tetravalent cation.[14] Furthermore, the respective species allow a number of conformations owing to the freedom of rotation in the four pyridyl units, all of which cannot be coplanar at once with the pyrazine because of the steric hindrance.[13] In both Hxa salts, the molecules are diprotonated as H_2-$TPPZ^{2+}$. The H_2-$TPPZ^{2+}$ acts as a proton sponge by forming intramolecular hydrogen bridges between the respective two pyridyl nitrogen atoms with a very short $N\cdots N$ distance (Figure 8b). All the pyridyl rings are somewhat twisted against the central pyrazine moiety. The two $NH\cdots N$ bridges are displaced to opposite sides of the pyrazine ring plane, as shown in Figure 8b. This conformation is the same as the "bowed" shape in the tetraphenylborate salt but differs from the "twisted" shape observed in the triiodide salt.[14a] Here we focus on the effect of phase transition on the molecular structures, demonstrating a breaking of molecular symmetry by changing the proton locations and twisting degree of the pyridyl units.

3.6.1. Nonpolar Geometry in Paraelectric (FE) Structure. Since the H_2-$TPPZ^{2+}$ molecule is located on an inversion center, its asymmetric unit has only one $NH\cdots N$ bridge in the PE structure. The $N\cdots N$ distance is commonly 2.55 Å in both the Hca and Hba salts. As indicated by the elongated N−H distance (1.15−1.20 Å), the refined proton position approaches the middle of the two nitrogen atoms, and this strong hydrogen-bonding may thus be formulated as $N\cdots H^+\cdots N$. The intermediate character between the protonated and unprotonated forms is also evident in the pyridine *ipso* angle (∠CNC), which is found to increase from 117° to 123° upon protonation.[27] In each compound, the ∠CNC differs by less than 1° between the inequivalent rings 1 and 2 (121−122°) shown in Chart 2, the delocalized protons suggesting their averaged environment. The delocalized picture was confirmed by the differential MEM analysis. Figure 11a exhibits a contour map calculated on a plane defined by the pyridyl nitrogen and adjacent carbon atoms, shown by a yellow trapezoid in Figure 11b. The electron is broadly distributed around the middle of hydrogen bond, and a slight splitting into double maxima indicates the positional disorder of the hydrogen in the PE phase. It should be noted

(24) Ishida, H.; Kashino, S. *Acta Crystallogr. C* **1999**, *55*, 1149–1152.
(25) (a) Ishida, H.; Kashino, S. *Z. Naturforsch.* **2002**, *57a*, 829–836. (b) Ishida, H. *Acta Crystallogr. E* **2004**, *60*, o1674−1676. (c) Fukunaga, T.; Ishida, H. *Acta Crystallogr. E* **2003**, *59*, o1793−1795. (d) Ishida, H.; Kashino, S. *Acta Crystallogr. C* **2000**, *56*, e202−204.
(26) Andersen, E. K. *Acta Crystallogr.* **1967**, *22*, 196–201.
(27) Majerz, I.; Koll, A. *Acta Crystallogr. B* **2004**, *60*, 406–415.

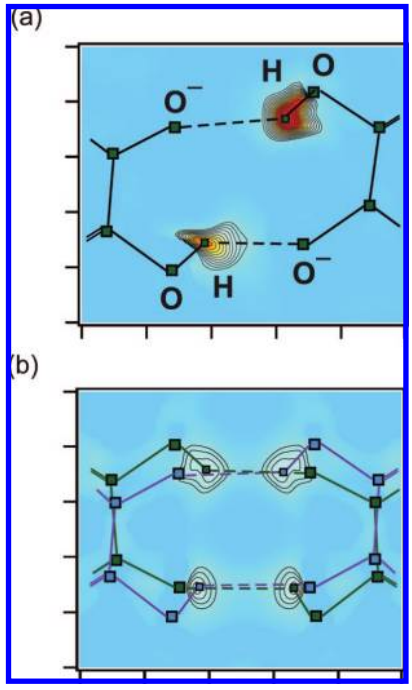

Figure 10. Thermal changes of the O−H···O⁻ bonds on the $[Hca^-]_2$ dimer in $[H_2\text{-TPPZ}][Hca]_2$. Electron density distributions deduced by the differential MEM analysis show (a) the ordered protons in the ferroelectric phase (FE structure, $T = 100$ K) and (b) the thermally disordered protons in the paraelectric phase (PE structure, $T = 295$ K). Contour curves are calculated on a least-squares plane defined by the surrounding oxygen atoms drawn from 0.2 to 1.0 e Å^{-3} with a constant interval (0.05 e Å^{-3}).

that the refined position of the hydrogen is located between these two maxima.

3.6.2. Polar Geometry in Ferroelectric (FE) Structure. In the FE structure, the H_2-$TPPZ^{2+}$ dication loses the C_i molecular symmetry, and then the entire molecule is crystallographically independent. One NH···N bridge is shortened (designated as the *a*-site hereafter) and the other is elongated (*b*-site) in the N···N distance compared with the PE structure (Table 2). This origin is reasonably related to the increasing or decreasing twisting angle ψ between the corresponding pyridine and pyrazine rings, as drawn in Chart 2. The twisting rotation thus represents the deformation of the H_2-$TPPZ^{2+}$ molecule. This also affects the hydrogen distributions. The *a*-site has the longer N−H distance (Table 2) and preserves a disordered character, as revealed by the doubly split electron distribution in the differential MEM analysis (Figure 11c) as well as the almost identical pyridine *ipso* angles (Table 2) between the pyridyl rings 1a and 2a. For the *b*-site, by contrast, the shortened N−H distance and evolving difference in ∠CNC clearly distinguish the rings 1b and 2b as the neutral and protonated forms, respectively. The proton localization in N^+−H···N form is evident on ring 2b also from the differential MEM analysis (Figure 11c).

The above observations are qualitatively explained by the potential curve of the N^+−H···N bridge, which has been predicted to change from double minima with quite shallow energy barriers to a broad single minimum upon shortening the N···N distance from 2.6 to 2.5 Å.[12a] That is, the proton delocalization could be facilitated in the *a*-site by the further flattened potential curve due to the N···N distance being shortened from 2.55 to 2.53 Å. By contrast, in the *b*-site, the increased separation from 2.56 to 2.57 Å would lift the potential

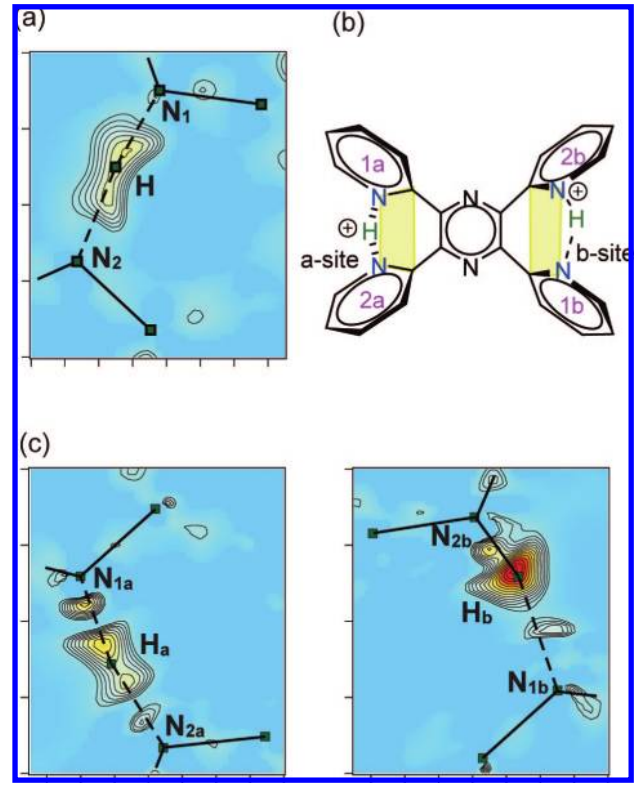

Figure 11. Thermal changes of the NH···N bridges on the H_2-$TPPZ^{2+}$ molecule in $[H_2\text{-TPPZ}][Hca]_2$. (a) Electron density distributions in paraelectric phase (PE structure, $T = 295$ K) deduced by the differential MEM analysis. Contour curves are drawn from 0.2 to 1.0 e Å^{-3} with a constant interval (0.05 e Å^{-3}). (b) Labeling of the sites on the H_2-$TPPZ^{2+}$ molecule with asymmetric location of protons and definition of the cross sections (yellow trapezoid) for mapping which are formed by pyridyl nitrogen and the adjacent carbon atoms. (c) Electron density distributions in the ferroelectric phase (FE structure, $T = 100$ K) for the *a*- (left) and *b*-sites (right).

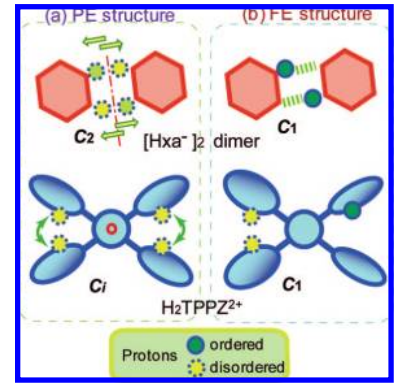

Figure 12. Schematic drawings of (a) the nonpolar molecular geometries in the PE structure and (b) the polar ones in the FE structure. The ordered and disordered protons are shown by the solid and dotted circles, respectively.

barrier between the double minima and consequently favor the proton's localization on one side. Such partial proton ordering characterizes the symmetry breaking of the H_2-$TPPZ^{2+}$ dication, as schematically shown in Figure 12.

3.7. Microscopic Effect of High Electric Field. In order to confirm the polarization reversal on a microscopic level, we performed X-ray structural analysis on an electrically poled single crystal. The absolute structure of the polar and/or chiral system is generally assessed by refinement of Flack's param-

Table 3. Calculated Dipole Moments (Debye per Formula Unit) and Spontaneous Polarization of $[H_2\text{-TPPZ}][Hxa]_2$[a]

	$[H_2\text{-TPPZ}][Hba]_2$				$[H_2\text{-TPPZ}][Hca]_2$			
	a	*b*	*c*	total	*a*	*b*	*c*	total
displacement, p_{ion}	+0.1351	0	−0.4771	0.479	−0.1679	0	+0.6086	0.611
local dipoles, p_{dipole}	−1.8960	0	−0.0489		+0.9142	0	−0.3054	
$H_2\text{-TPPZ}^{2+}$, p_{tppz}	−2.0214	−5.6968	−0.6291	6.131	+0.9218	−2.7576	+0.4171	2.971
$[Hxa^-]_2$, p_{Hxa2}	+0.1254	+0.0127	+0.5802	0.627	−0.0076	−0.0514	−0.7225	0.758
(unoptimized)	−0.3353	−0.0688	+0.6578	0.696	+1.0029	−0.1780	−1.5494	1.714)
total, p_{total}	−1.7609	0	−0.5260		+0.7463	0	+0.3032	
P_s^{calc} (μC cm^{-2})	−0.709	0	−0.212		+0.310	0	+0.126	
$P_{s[110]}$ (μC cm^{-2})	0.12				0.062			

[a] See text for definitions of p_{total}, p_{ion}, and p_{dipole}. $P_s^{calc} = 4p_{total}/V$.

eter,[20] which represents a fraction of the inverted structure varying from 0 to 1. For the as-grown crystals without poling, Flack's parameters were typically 0.4−0.6, indicative of the coexistence of both polarizations with nearly equal fractions. When the crystals were cooled from the PE state under dc bias field of 1.3 kV cm^{-1} applied parallel to the crystallographic [110] direction, Flack's parameters were nearly zero: 0.05(2) for $[H_2\text{-TPPZ}][Hba]_2$ and 0.10(2) for $[H_2\text{-TPPZ}][Hca]_2$. Under an inverted bias, these values increased to 0.95(2) and 0.76(2), respectively, indicating the reversed polarity. These observations unambiguously prove the forced alignment and reversal of spontaneous polarization under applied electric field. The correspondence between the observed absolute configuration and the bias-field direction herein has also justified the polarity of the dipole moments calculated below using atomic coordinates of the FE structure with either absolute configuration.

3.8. Dipole Moments of the FE Structures. Due to the *c*-glide plane symmetry in the *C*-centered monoclinic lattice, the bulk polarization of the FE structures is canceled out in the *b*-component and hence parallel to the *ac* plane. As the relevant contributions, both the H_2-TPPZ dication and the $[Hxa^-]_2$ dimer attain the dipole moment more or less due to their respective proton ordering. Moreover, their relative displacement should also contribute to the net polarization. The comparison of their averaged atomic positions between the FE and PE structures gave the displacement along the *a*- and *c*-directions, $(\Delta x, \Delta z) = (-0.00022, +0.00329)$ and $(+0.00024, -0.00430)$ for the Hba and Hca salts, respectively. The resultant moment p_{ion} from the simple point-charge model appears principally along the molecular stacking *c*-directions, but its magnitude is not so large (Table 3).

Rather, larger contributions were found on the individual molecular dipoles. To estimate the dipole moments of both the H_2-TPPZ dication and the $[Hxa^-]_2$ dimer, semiempirical molecular orbital calculations were performed with the PM3 Hamiltonian and RHF method using the MOPAC program,[28] using the atomic coordinates obtained by X-ray analysis. Table 3 summarizes the respective *a*-, *b*-, and *c*-components of the respective dipole moments. Here, p_{dipole} per formula is defined as the total contribution from the all molecular dipoles in the unit cell and has zero *b*-component in the presence of the *c*-glide plane. One can easily expect that the coplanar $[Hxa^-]_2$ dimer would be the least polar. The actual slight twisting by 17−18° yields a small dipole approximately perpendicular to the dimer plane, as shown by the arrow in Figure 8a, and dominantly contributes to the *c*-component. Whereas the proton locations with unnaturally short O−H distances in the X-ray analysis (Table 2) somewhat overvalued the polarization, their correction with the energy-optimizing computation gave a modest polarization p_{Hxa2}, together with rational O−H lengths (0.97 Å).

On the other hand, the most important contribution to p_{dipole} arises from the H_2-TPPZ dipole p_{tppz}, as expected from the apparent asymmetric proton ordering. In both salts, the calculated p_{tppz} is nearly parallel to the NH···N bridges, as shown by an arrow in Figure 8b. Its major portions are canceled out by the *b*-component, but the modest *a*-component remains the most significant contribution to the bulk polarization. In agreement with the dielectric properties, the spontaneous polarization appears mostly along the *a*-direction, when calculated as $P_s^{calc} = 4(p_{ion} + p_{dipole})/V$, with *V* the unit-cell volume. However, the calculations (Table 3) still overrate the polarization, which cannot be solely attributed to a slight discrepancy in the field directions between [110] for the experimental P_s and [100] for the calculation. Rather, it should be related to the fact that the calculated dipoles change fairly sensitively with the proton locations. The computations are based on the refined proton locations, although the actual electron distribution maxima were found to exhibit a more delocalized nature of the hydrogens, even in the FE state, especially for the *a*-site. This might account for the diminished polarization in comparison to the calculated model. Accurate assignment of the spatial distribution of both electrons and protons for hydrogens with use of precise X-ray and neutron experiments would be indispensable for the further quantitative evaluation of the delicate contributions to the small polarization of the present compounds.

3.9. Possible Structural Origins of Dielectric Anomalies. The hydrogen-bonding protons should play crucial roles in the phase transition, as is evident from the significant deuteration effect on T_c. Therefore, the sizable difference in T_c between the two isomorphous salts may reflect the H-bonding geometry. In fact, the O···O distance in the Hca salt is about 0.02 Å shorter than that in the Hba salt, whereas the difference is less than 0.006 Å for the N···N distance (Table 2). The shortened O···O distance, which may result from the different packing effects, can reduce the potential barrier for double-proton transfer and hence explain the reduction of T_c in the Hca salt. The double-proton order couples closely with the moiety structure of the surrounding non-hydrogen atoms, as is evident in the random occupation of the moiety over the two possible directions, and hence should be the primal trigger of the structural phase transition. On the other hand, the dipole moments mostly arise from the acentric proton-ordering on the H_2-TPPZ dication, coupled with the twisting rotation of the pyridyl rings.

The structural inversion for ferroelectricity corresponds to an interchange between the *a*- and *b*-sites on the H_2-TPPZ dication thorough the transfer of bridging protons and also accompanies simultaneous twisting rotation of bulky pyridyl

(28) Stewart, J. J. P. *Int. J. Quantum Chem.* **1996**, *58*, 133–146.

units. Importantly, the inversion involves also a double-proton transfer on the $[Hxa^-]_2$ dimer. As noted above, the both processes should significantly modify the molecular geometry and orientations in the crystal. Such dynamic intermolecular distortions and reorientations involve the movement of heavy objects, and the resultant high potential barriers for thermally activated transition would extremely delay the polarization reversal, as observed.

In the $[Hxa^-]_2$ dimer, two protons are confined in the cyclic bond, and their dynamics should be tied with the π-electron system. In contrast, for the H_2-$TPPZ^{2+}$ dication, the two bridging protons are sufficiently apart in space from each other. Furthermore, the π-electron system is not extended between the neighboring twisted rings, and hence these protons would not communicate with each other originally. Rather, the asymmetric twisting of pyridyl units is seemingly driven by the molecular rotations of the surrounding $[Hxa^-]_2$ dimers during the double-proton transfer. This is suggested by the fact that each carbon atom at the 6-position of a pyridyl ring has a close atomic contact with either a halogen or carbonyl oxygen atom on the adjacent dimer. For instance, the FE structure of the Hba salt hosts the C···Br (3.31, 3.51 Å) and C···O distances (3.12, 3.14 Å), which are shorter than the sum of van der Waals radii.

4. Conclusion

The present work has demonstrated that both proton dynamics and the resultant ferroelectricity are realized with the hydrogen-bonding architectures distinct from the precedent ferroelectrics. The acid and base herein exist as the cyclic H-bonded dimer $[Hxa^-]_2$ and the diprotonated proton sponge H_2-$TPPZ^{2+}$, respectively, without inter-unit H-bonding. The symmetry-breaking phase transition involves two kinds of proton motions. Freezing of the double-proton transfer on the dimer is the most characteristic process. It appears to force significant orientational motion of the molecule, and the dynamics of the dimer could induce twisting deformation on the pyridyl units of the proton sponge through close inter-unit atomic contacts. The latter conformational change also leads to partial localization of the NHN bridge protons, and the resultant acentricity affords the spontaneous polarization. The ferroelectricity is thus a cooperative phenomenon between the base and acid, realized through the strong correlation between proton and molecular dynamics, a part of which processes should cause the slow polarization dynamics suggested by the dielectric properties.

Acknowledgment. This study was partly supported by a Grant-in-Aid for Scientific Research (no. 18750133) by the Ministry of Education, Culture, Sports, Science and Technology of Japan.

Supporting Information Available: Infrared and UV−vis spectra (PDF) and X-ray crystallography files (CIF). This material is available free of charge via the Internet at http://pubs.acs.org.

JA8032235